







Thermal fluctuation noise in Mo/Au superconducting transition-edge sensor microcalorimeters

Cite as: J. Appl. Phys. **125**, 164503 (2019); <https://doi.org/10.1063/1.5086045>

Submitted: 17 December 2018 . Accepted: 04 April 2019 . Published Online: 23 April 2019

N. A. Wakeham , J. S. Adams, S. R. Bandler , S. Beaumont, J. A. Chervenak, A. M. Datesman, M. E. Eckart, F. M. Finkbeiner, R. Hummatov , R. L. Kelley, C. A. Kilbourne , A. R. Miniussi , F. S. Porter, J. E. Sadleir, K. Sakai , S. J. Smith, and E. J. Wassell



View Online



Export Citation



CrossMark

ARTICLES YOU MAY BE INTERESTED IN

[Superconducting transition edge sensors with phononic thermal isolation](#)

Journal of Applied Physics **124**, 144501 (2018); <https://doi.org/10.1063/1.5041348>

[Nanoscale thermal characterization of high aspect ratio gold nanorods for photothermal applications at \$\lambda=1.5\mu\text{m}\$](#)

Journal of Applied Physics **125**, 163101 (2019); <https://doi.org/10.1063/1.5088944>

[Optimization of Al/AIO_x/Al-layer systems for Josephson junctions from a microstructure point of view](#)

Journal of Applied Physics **125**, 165301 (2019); <https://doi.org/10.1063/1.5089871>

Lock-in Amplifiers up to 600 MHz

starting at

\$6,210



 Zurich
Instruments

Watch the Video









Thermal fluctuation noise in Mo/Au superconducting transition-edge sensor microcalorimeters

Cite as: J. Appl. Phys. **125**, 164503 (2019); doi: [10.1063/1.5086045](https://doi.org/10.1063/1.5086045)

Submitted: 17 December 2018 · Accepted: 4 April 2019 ·

Published Online: 23 April 2019



N. A. Wakeham,^{1,2,a)}  J. S. Adams,^{1,2} S. R. Bandler,¹  S. Beaumont,^{1,2} J. A. Chervenak,¹ A. M. Datesman,^{1,3} M. E. Eckart,⁴ F. M. Finkbeiner,^{1,5} R. Hummatov,^{1,2}  R. L. Kelley,¹ C. A. Kilbourne,¹  A. R. Miniussi,^{1,2}  F. S. Porter,¹ J. E. Sadleir,¹ K. Sakai,^{1,2}  S. J. Smith,^{1,2} and E. J. Wassell^{1,3}

AFFILIATIONS

¹Goddard Space Flight Center (GSFC), NASA, Greenbelt, Maryland 20771, USA

²CRESST II—University of Maryland Baltimore County, Maryland 21250, USA

³KBRwyle, Lexington Park, Maryland 20653, USA

⁴Lawrence Livermore National Laboratory (LLNL), Livermore, California 94550, USA

⁵Sigma Space Corp., 4600 Forbes Blvd., Lanham, Maryland 20706, USA

^{a)}Electronic mail: nicholas.a.wakeham@nasa.gov

ABSTRACT

In many superconducting transition-edge sensor (TES) microcalorimeters, the measured electrical noise exceeds theoretical estimates based on a thermal model of a single body thermally connected to a heat bath. Here, we report on noise and complex impedance measurements of a range of designs of TESs made with a Mo/Au bilayer. We have fitted the measured data using a two-body model, where the x-ray absorber and the TES are connected by an internal thermal conductance G_{ae} . We find that the so-called excess noise measured in these devices is consistent with the noise generated from the internal thermal fluctuations between the x-ray absorber and the TES. Our fitted parameters are consistent with the origin of G_{ae} being from the finite thermal conductance of the TES itself. These results suggest that even in these relatively low resistance Mo/Au TESs, the internal thermal conductance of the TES may add significant additional noise and could account for all the measured excess noise. Furthermore, we find that around regions of the superconducting transition with rapidly changing derivative of resistance with respect to temperature, an additional noise mechanism may dominate. These observations may lead to a greater understanding of TES devices and allow the design of TES microcalorimeters with improved performance.

© 2019 Author(s). All article content, except where otherwise noted, is licensed under a Creative Commons Attribution (CC BY) license (<http://creativecommons.org/licenses/by/4.0/>). <https://doi.org/10.1063/1.5086045>

I. INTRODUCTION

An ideal photon detecting microcalorimeter consists of a photon absorber coupled to a sensitive thermometer, with the heat capacity and temperature sensitivity of the device chosen to optimize the energy resolving power at the target photon energy. In practice, the thermometer in these microcalorimeters can be realized using a superconducting transition-edge sensor (TES), which consists of a thin metallic film cooled to low temperatures and voltage biased into the transition between the normal and superconducting state. In a TES microcalorimeter, the absorption of a photon in the device causes a change in the TES temperature and, therefore,

resistance, which can be detected as a change in the measured current. TES microcalorimeters are the baseline technology, or are currently deployed, in a host of measurement applications including nuclear material security,¹ elemental content analysis,² atomic physics,³ particle physics,⁴ and astronomy.^{5,6} A great advantage of TES microcalorimeters is their excellent energy resolution over a wide range of incident photon energies. However, one limitation on the energy resolution of a given TES microcalorimeter is the magnitude of the noise in the measurement circuit.

While much of the measured noise in TES microcalorimeters is from known sources, such as the Johnson noise and thermal

fluctuations between the device and the thermal bath, it has been observed previously that in many device designs, the measured noise is in excess of these known sources.^{7–10} Extensive work tracing the source of this so-called “excess noise,” and its dependence on various parameters, has revealed that it is highly sensitive to the details of the TES design and properties of the superconducting resistive transition.^{8,11} There have been many papers describing the theoretical predictions for the noise in real devices based on multibody thermal models^{12,13} or physical properties of the TES itself when biased in the superconducting transition.^{14–17} Indeed, in some particular cases, explanations of additional noise sources have been found. In highly resistive devices, it was shown that thermal fluctuation noise internal to the microcalorimeter may be a significant contribution.^{18–20} In test structures designed for studying the noise terms, rather than in viable microcalorimeters, it was shown that noise may arise from separate regions of the TES being in superconducting and normal states.²¹

Here, we report on a description of the measured noise in Mo/Au bilayer TES microcalorimeters made at NASA Goddard Space Flight Center that are the baseline technology for the X-ray Integral Field Unit on the Advanced Telescope for High-Energy Astrophysics (Athena) mission.⁵ This type of TES device has shown excellent energy resolution, both in single-pixels²² and in kilo-pixel TES arrays with multiplexed readout.²³ Even in these devices, capable of <2 eV resolution at 6 keV, there is significant excess noise that has not been explained.^{8,10} An explanation for this excess noise may allow design modifications in these, and other TES devices, to give significantly reduced noise, improved performance, and an improved understanding of thermal transport within the microcalorimeter. This is particularly relevant to devices without metal features added on top of the TES that have high sensitivity of the resistance to temperature, which have recently been shown to have smooth and highly reproducible transition shapes.¹⁰

In this article, Sec. II describes the TES design and the experimental techniques used to measure various properties of the microcalorimeters. Section III gives a summary of the thermal models used in this work that were developed by many others.^{12,13,24} First, we describe the simple “single-body” electrothermal model of the devices that demonstrates the measured noise in excess of this simple prediction. Next, we describe the “two-body” model, where the TES and the absorber are separated into two thermal bodies. We then apply this two-body model to our devices to determine if it is consistent with the observed excess noise. Section IV describes the measured excess noise in our devices and how well the two-body model is able to account for that excess noise. Section V describes the physical interpretation of the fitted parameters in our model and how this may lead to designs with improved performance, and deeper understanding of the important physical parameters in these devices.

II. METHOD

The current design of the superconducting TES microcalorimeter produced at NASA has an x-ray absorber made up of an electroplated Bi layer ($\sim 3\mu\text{m}$ thick) above a Au layer ($\sim 2\mu\text{m}$ thick). This square absorber with $240\mu\text{m}$ side length is then thermally connected to a superconducting Mo/Au bilayer by two pillar

shaped Au stems ($\sim 4\mu\text{m}$ tall, $10\mu\text{m}$ diameter) at the edge of the TES. These pillar stems either connect directly to the Mo/Au bilayer, or they connect to Au banks that run parallel to the current direction along the edge of the TES, as shown in Fig. 1. The bilayer sits in the center of a larger silicon nitride membrane, which extends to a Si frame that is well heat sunk and forms the heat bath. The TES bilayer is electrically connected with Nb leads. The TES designs discussed here are square with the side length ranging from 75 to $120\mu\text{m}$. We will discuss measurements of devices with one of two bilayer thicknesses. The thicker low resistance devices have a Mo/Au bilayer thickness of $51/252$ nm and a low temperature sheet resistance of $13\text{ m}\Omega/\square$. The thinner high resistance devices have a Mo/Au thickness of $35/108$ nm and a sheet resistance of $50\text{ m}\Omega/\square$. Details of the TES design and fabrication are discussed elsewhere.^{8,10}

A host of measurements were performed on these devices using the circuit shown in Fig. 2. The complex impedance of the TES was measured in the range of 10 Hz – 5 kHz . The TES was voltage biased such that the TES resistance R was a fixed fraction of the normal state resistance R_N . In parallel to this, a function generator was used to apply a small alternating bias to the TES circuit at different fixed frequencies. This alternating bias input and the current through the TES were measured using the same digitizer with identical low-pass filtering and used to determine the total impedance of the circuit. Measurements with zero direct bias voltage, and hence the TES in the superconducting state, were used to fit the inductance of the circuit to allow determination of the TES impedance. These measurements can be used to determine the sensitivity of R to changes in TES temperature T and current I , parameterized by $\alpha = (T/R)(\partial R/\partial T)|_I$ and $\beta = (I/R)(\partial R/\partial I)|_T$.²⁵ The thermal conductance was measured from fitting the Joule heating power in the TES when biased to 50% of R_N at various bath temperatures. The choice of the bias point used in the power fitting has a small impact on the fitted thermal conductance in these devices but does not significantly alter any of the conclusions drawn in this article. The heat capacity of each device was calculated from the measurement of the thermal decay time constant of the device after absorption of an x-ray in the absence of electrothermal feedback at a bath temperature above the superconducting transition temperature

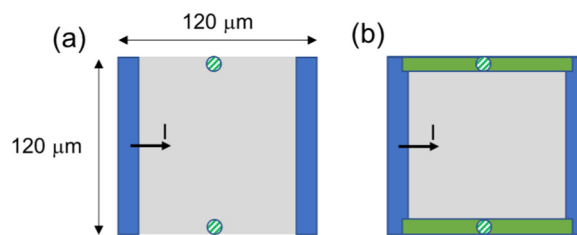


FIG. 1. Schematic diagram of $120\mu\text{m}$ TES devices viewed from above. Absorbers are not shown for clarity. Mo/Au bilayer is shown in gray, and electrical connection is made with Nb leads shown in blue. Bi/Au absorbers are attached with Au pillars shown as green hatched circles. TES is shown (a) without and (b) with Au banks (solid green) placed parallel to the direction of the current I .

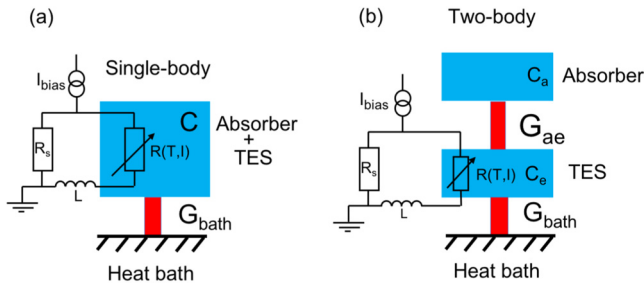


FIG. 2. Schematic diagram of (a) a single-body and (b) a two-body thermal model of the TES microcalorimeter with the electrical circuit also shown.

T_c . Current noise spectra were calculated from the Fourier transform of measurements of the current through the TES. These were measured with a superconducting quantum interference device (SQUID) with a 250 kHz Bessel low-pass filter of 12 dB/Oct. All measurements discussed in this article were performed with the application of a small magnetic field perpendicular to the TES to null this component of the small external field trapped in the apparatus. These methods are well established and are described in detail elsewhere.^{8,26}

III. ELECTROTHERMAL MODELS

The simplest electrothermal model to describe the measured electrical noise and complex impedance of a TES is a single-body model shown schematically in Fig. 2(a). This model consists of a single element with heat capacity C thermally connected to a heat bath by thermal conductance G_{bath} . The single element here incorporates the absorber and the TES bilayer. In the small signal limit, which is applicable to noise and complex impedance measurements, where the change in TES temperature $\Delta T \ll T$ and change in TES current $\Delta I \ll I$, the single-body model can be described by two linearized differential equations²⁵

$$\frac{d}{dt} \begin{pmatrix} \Delta I \\ \Delta T \end{pmatrix} = \begin{bmatrix} -(1/L)[R(1 + \beta) + R_s] & -(\alpha IR/LT) \\ (2 + \beta)(IR/C) & (1/C)[(\alpha I^2 R/T) - G_{bath}] \end{bmatrix} \times \begin{pmatrix} \Delta I \\ \Delta T \end{pmatrix}, \quad (1)$$

where R_s and L are the shunt resistance and circuit inductance, respectively, as shown in Fig. 2(a).

Frequency dependent analysis can be obtained from considering harmonic solutions, with angular frequency ω , to the differential equations, and again linearizing to give

$$\begin{bmatrix} R(1 + \beta) + R_s + i\omega L & -(\alpha IR/LT) \\ -(2 + \beta)(IR) & G_{bath} - (\alpha I^2 R/T) + i\omega C \end{bmatrix} \times \begin{pmatrix} \Delta I \\ \Delta T \end{pmatrix} = \begin{pmatrix} e_{tes} + e_{shunt} \\ p_{bath} - Ie_{tes} \end{pmatrix}. \quad (2)$$

In this single-body model, there are three intrinsic contributions to the electrical noise measured in the TES. The first is the thermal

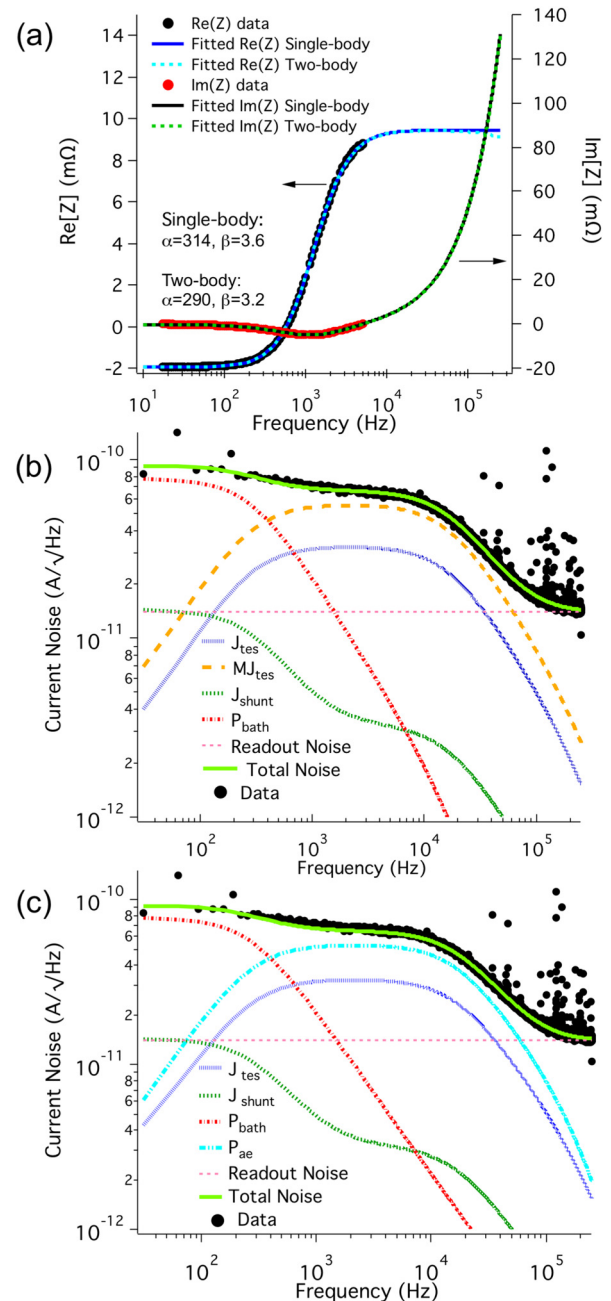


FIG. 3. Comparison of complex impedance and noise data fitting with the single-body and two-body models. (a) Points show complex impedance of the TES Z extracted from the measured circuit impedance. Lines show fitted impedance from the single-body model (solid) and the two-body model (dashed). Fitted parameters for each model are shown. In (b) and (c), black points show the current noise spectrum measured for a $120 \mu\text{m}$ high resistance TES without banks biased at $R/R_N = 5\%$ at $T_{bath} = 55 \text{ mK}$. (b) Lines show intrinsic noise sources calculated using the single-body model and a fitted excess noise term MJ_{tes} . (c) Lines show intrinsic noise sources calculated using the two-body model with $G_{ae}(T_c) = 100 \text{ nW/K}$.

fluctuation noise between the single body and the heat bath p_{bath} . This is considered as a white thermal noise given for the specular limit by $p_{bath} = \sqrt{2k_b T^2 G_{bath} ((T_{bath}/T)^{\beta_G+2} + 1)}$, where β_G is the exponent of the temperature dependence of G_{bath} .^{27,28} The second is the white voltage noise from the Johnson noise of the shunt resistor in the TES readout circuit that is connected in parallel with the TES $e_{shunt} = \sqrt{4k_b T_{bath} R_s}$. The third is from the nonequilibrium Johnson noise from the TES itself when it is biased within the superconducting transition $e_{tes} = \sqrt{4k_b TR(1 + 2\beta)}$.¹⁴

The inverse of the matrix in Eq. (2) gives the responsivity of the system. This can then be used to calculate α and β from measurements of the complex impedance of the TES.²⁵ An example of the measured complex impedance of the TES and the single-body fit is shown in Fig. 3(a). Equation (2) can also be used to calculate the current noise measured in the TES circuit from each of the different noise sources. The current noise from the thermal fluctuations, shunt resistor Johnson noise, and TES nonequilibrium Johnson noise is given by P_{bath} , J_{shunt} , and J_{tes} , respectively. An example of these current noise terms in the TES is shown in Fig. 3(b).

It has been shown previously that the measured noise in real devices exceeds the expectations from the quadrature sum of the three known single-body contributions, particularly in the region from 1 to 250 kHz.⁷⁻¹⁰ This has led to the discussion of an additional “excess” noise in the system. To quantify the magnitude of the excess noise term, it is often assumed to arise from an additional term in the TES Johnson noise, such that $e_{tes} = \sqrt{4k_b TR(1 + 2\beta)(1 + M^2)}$ where M is a unitless arbitrary scaling factor.⁸ This means that the excess current noise is given by MJ_{tes} . The value of M^2 can be fitted such that when added to the known single-body noise terms and readout noise, the measured and total predicted noise spectra agree. Thus, M^2 is a parameter that quantifies how much the measured

noise exceeds the sum of the known single-body noise sources. This is shown in Fig. 3(b) for a 120 μm TES without banks biased into the transition at $R/R_N = 5\%$ at $T_{bath} = 55$ mK. The fitting excludes the interference noise spikes at 60 and 120 Hz and is weighted by $1/\log(\omega)$ to account for the logarithmic increase in density of data points with increasing frequency. The only free parameters in the fit are the value of M and the magnitude of the readout noise.

By adding the fitted excess noise term, the total calculated noise and measured noise spectra have been shown to largely agree for a wide range of TES devices,^{8,11} but such an arbitrary fitting does not elucidate the source of the noise. The ability to satisfactorily fit the measured noise of devices by the addition of a term with the frequency dependence of the Johnson noise has led to the suggestion that this excess noise is the result of higher order terms not typically included in expressions for nonequilibrium Johnson noise. Others have suggested that the noise results from changes in phase-slip lines across the TES.^{15,16} In some high resistivity devices, it has been argued that the noise is dominated by thermal fluctuation noise between different parts of the microcalorimeter^{18,19} or between normal and superconducting regions of the TES bilayer.²¹

A more complex model of the microcalorimeter is the two-body model shown in Fig. 2(b). In this model, one body is assumed to be thermally connected, with conductance G_{ae} , to a second body that is connected directly to the heat bath. Here, we assign the top body to the absorber and the lower body to the TES. The absorber has heat capacity C_a and the TES has heat capacity C_e . As discussed above, the total heat capacity of the microcalorimeter pixel is measured for each device. We assume here that this measured value C_{meas} is the sum of the two components $C_{meas} = C_a + C_e$ and G_{bath} is the measured thermal conductance for each pixel. The linearized differential equations for this model are given by^{12,13}

$$\frac{d}{dt} \begin{pmatrix} \Delta I \\ \Delta T_e \\ \Delta T_a \end{pmatrix} = \begin{bmatrix} -(1/L)[R(1 + \beta) + R_s] & -(\alpha IR/LT_e) & 0 \\ (2 + \beta)(IR/C_e) & -[G_{bath} + G_{ae}^{tes} - (\alpha I^2 R/T)]/C_e & G_{ae}^a/C_e \\ 0 & G_{ae}^{tes}/C_a & -G_{ae}^a/C_a \end{bmatrix} \begin{pmatrix} \Delta I \\ \Delta T_e \\ \Delta T_a \end{pmatrix}, \quad (3)$$

where the superscripts on the thermal conductance terms indicate at which body the temperature is used in the evaluation of the thermal conductance.

In the two-body model, there is an additional white thermal fluctuation noise term p_{ae} into each of the two bodies defined in analogy to p_{bath} . These fluctuations are observed as the current noise term P_{ae} . Figure 3(c) shows the same measured noise spectrum as Fig. 3(b) but now fitted with this two-body model, assuming the same readout noise level as the single-body case. The observed excess noise can now be ascribed to this internal thermal fluctuation noise. The two-body model can also be used to calculate α and β from the complex impedance, as shown in Fig. 3(a). In general, these parameters calculated with the two-body model need not agree with those parameters extracted from the single-body model. However, note that in this case, the difference between the two models is small except at very high frequencies.

As an aside, note that in Figs. 3(b) and 3(c), P_{bath} is increased by $\sim 20\%$ from the theoretical predictions to ensure a good fit to data at very low frequencies (<1 kHz). The origin of this additional noise is not known. It may be the result of thermal radiation on the detector from higher temperature regions of the cryostat during the measurement. A power into the absorber of ~ 0.7 pW is estimated to be sufficient to raise the magnitude of the low frequency noise level to match the data. The increased low frequency noise may also be the consequence of even greater complexity of the thermal connections of the device not considered here. In this article, we focus on the excess noise at higher frequencies in the range of 1–250 kHz that has previously been described with an M^2 parameter. This is above the frequency range where the additional P_{bath} is dominant, as shown in Figs. 3(b) and 3(c), and therefore, the lower frequency noise is largely irrelevant for the discussions that follow.

IV. RESULTS

To begin, we have fitted noise and complex impedance data from two devices without banks with the high resistance bilayer (sheet resistance $50 \text{ m}\Omega/\square$) using the single-body model. Figures 4(a) and 4(b) show α and β , respectively, as a function of TES resistance extracted from single-body fitting of the complex impedance data of a $120 \mu\text{m}$ TES without banks. Figure 4(c) shows the excess noise parameter M^2 extracted from fitting noise data with the single-body model. A comparison of Figs. 4(a) and 4(c) shows the broad correlation between M^2 and α that has been discussed before. Figure 4(d) shows M^2/α and demonstrates the reduction of this ratio with increasing bath temperature. Figure 5 shows the same single-body fitted parameters from noise and complex impedance measurements of a $75 \mu\text{m}$ TES with the same high resistance bilayer. Note again, the correlation between M^2 and α in Figs. 5(a) and 5(c), and the reduction in M^2/α with increasing bath temperature in Fig. 5(d). By comparing Figs. 4(d) and 5(d) at a fixed T_{bath} , we find that M^2/α is significantly larger for the $120 \mu\text{m}$ TES than for the $75 \mu\text{m}$ TES.

Let us now consider whether the variations in the excess noise between devices with different TES sizes and with T_{bath} may be

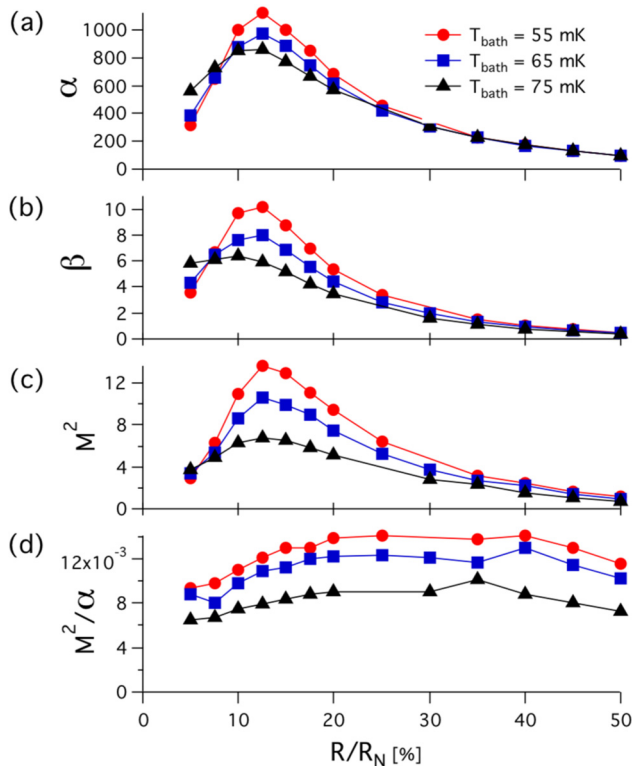


FIG. 4. Noise and transition parameters extracted by fitting the single-body model to data from a $120 \mu\text{m}$ high resistance TES without banks at various values of T_{bath} , as a function of the bias point in the transition R/R_N . Transition parameters (a) α and (b) β extracted from complex impedance measurements. (c) Excess noise parameter M^2 . (d) Ratio of M^2/α .

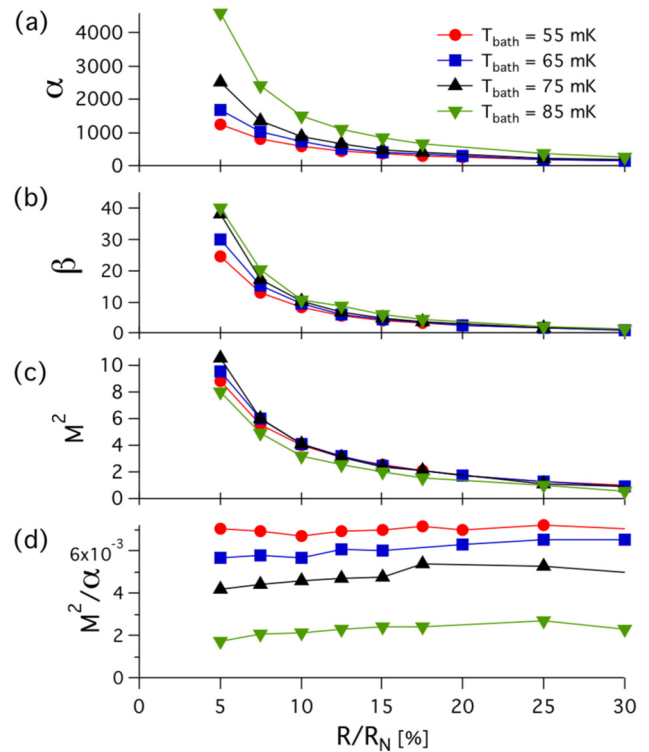


FIG. 5. Noise and transition parameters extracted by fitting the single-body model to data from a $75 \mu\text{m}$ high resistance TES without banks at various values of T_{bath} , as a function of the bias point in the transition R/R_N . Transition parameters (a) α and (b) β extracted from complex impedance measurements. (c) Excess noise parameter M^2 . (d) Ratio of M^2/α .

explained using the two-body model. We first make some assumptions about the properties of the absorber and the TES defined in our model. First, we assume that C_e is given by the BCS prediction of the TES bilayer at the peak of the superconducting jump at T_c for the particular dimensions of each TES pixel (typically $\sim 0.05 \text{ pJ/K}$), and a contribution from the membrane estimated from previous studies and kept constant at 0.01 pJ/K for all devices.²⁹ This BCS prediction is likely an upper limit on the heat capacity of the TES because the bilayer is a thin film and not a bulk material, and disorder/inhomogeneity in the superconducting film may act to reduce the size of the jump in the heat capacity at T_c . In addition, the proximity effect of the superconducting leads on the TES is predicted to reduce the magnitude of the superconducting jump from the BCS prediction.³⁰ The other parameters of our model are largely insensitive to the reduction of C_e , as shown in the [supplementary material](#). The total measured heat capacity is typically $\sim 1.2 \text{ pJ/K}$ and, therefore, $C_a \gg C_e$. Initially, we also assume that G_{ae} is not a function of R/R_N or of T_{bath} . This means that G_{ae} is simultaneously optimized to best fit all data for a single-pixel design at all values of R/R_N and T_{bath} . Later, we will consider the impact of removing this constraint.

Figure 3(c) shows a fit of the noise spectrum under these assumptions at a single bias point. The two-body model fits the

data well and it can be seen that this is because the P_{ae} term adds significantly to the total noise above 1 kHz. By comparing the J_{tes} and P_{ae} terms in the figure, it is also clear that the frequency dependence of each term is very similar. This conveniently allows us to parameterize the magnitude of the P_{ae} term by scaling it relative to the J_{tes} term with parameter Q , such that $P_{ae} \approx QJ_{tes}$. This means that while the M parameter describes the magnitude of the noise in excess of the known single-body model noise sources, the Q parameter describes the magnitude of the P_{ae} term. Therefore, if the thermal fluctuation noise between the absorber and the TES accounts for all the excess noise measured in our devices, then M^2 , extracted from the fitting of the single-body model with the excess Johnson noise term, will be equal to Q^2 extracted from fitting the two-body model.

Figure 6 shows the single-body noise parameter M^2 , and two-body noise parameter Q^2 , extracted from our measured data assuming constant $G_{ae}(T_c) = 100$ nW/K for all R/R_N and T_{bath} in the $120\ \mu\text{m}$ high resistance device. We find reasonable agreement between M^2 and Q^2 over a wide range of T_{bath} and R/R_N . Also, the quality of fit between our two-body model and the measured frequency dependent current noise shown in Fig. 3(c) is typical of all points represented in Fig. 6. This implies that despite being highly constrained, our two-body model, and in particular the additional P_{ae} term, is able to account for the measured excess noise in this device. The two-body model is also largely able to capture the dependence of excess noise on α , R/R_N , and T_{bath} discussed above.

The agreement between the M^2 and Q^2 extracted from the measured data is clearly not perfect at all points. This is particularly evident in the case of the $75\ \mu\text{m}$ device shown in Fig. 7 for

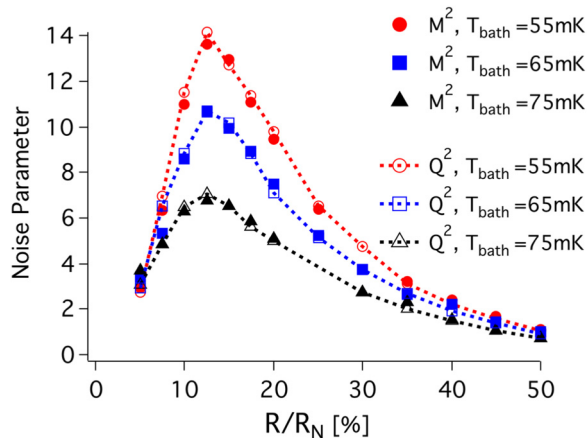


FIG. 6. Fitted noise parameters from single- and two-body models as a function of the bias point in the transition R/R_N at different values of T_{bath} for $120\ \mu\text{m}$ high resistance TES without banks. Closed symbols show excess noise parameter M^2 fitted in the single-body model also shown in Fig. 4. Open symbols show the magnitude of internal fluctuation noise parameter Q^2 calculated from the two-body model with constant G_{ae} for all T_{bath} and R/R_N . Exact agreement between open and closed symbols would indicate that the observed excess noise is well described by the internal thermal fluctuation noise in the two-body model.

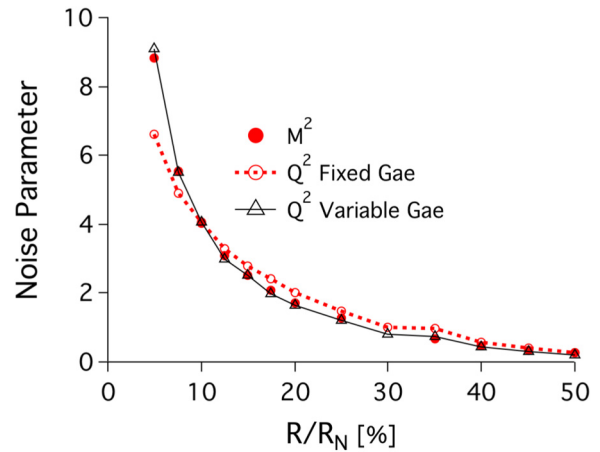


FIG. 7. Fitted noise parameters from single- and two-body models as a function of the bias point in the transition R/R_N for $75\ \mu\text{m}$ high resistance TES without banks at $T_{bath} = 55$ mK. Closed symbols show excess noise parameter M^2 fitted in the single-body model also shown in Fig. 5. Open symbols show the magnitude of internal fluctuation noise parameter Q^2 calculated from the two-body model with constant G_{ae} for all R/R_N (red circles), or with G_{ae} chosen for best fit to noise data at each value of R/R_N (black triangles). Exact agreement between open and closed symbols would indicate that the observed excess noise is well described by the internal thermal fluctuation noise in the two-body model.

$T_{bath} = 55$ mK. Here, we see that although the general trend of $M^2(R)$ is captured from the model, the two-body model with fixed G_{ae} underestimates the excess noise at small R/R_N (large α) and overestimates it at large R/R_N (small α). If we now allow G_{ae} to be a free parameter in our model, we can then fit the measured noise data with the two-body model at all bias points. This is shown by the agreement between M^2 and Q^2 calculated with variable G_{ae} , shown with the black triangles in Fig. 7. Note that because of the relative insensitivity of the noise spectra to a reduction in C_e , the change in excess noise through the transition cannot be fit by a reduction in C_e lower in the transition, and therefore, we keep C_e constant throughout.

This fitting of the two-body model with variable G_{ae} was performed on 75 , 100 , and $120\ \mu\text{m}$ TESs, some with banks, some without banks on both high and low resistance bilayers with $T_{bath} = 55$ mK. The noise spectra can in general be well fit by this model. The variation in the fitted G_{ae} is shown in Fig. 8 as a function of R/R_N . Let us focus first on the high resistance devices. The variation in the fitted G_{ae} with devices of different sizes is small. Note also that the difference between the fitted G_{ae} for $75\ \mu\text{m}$ devices with and without banks is within the variation seen between sizes. We also see that the fitted G_{ae} appears significantly lower at small R/R_N in all devices.

There is a striking difference between the fitted G_{ae} for high resistance bilayers, shown in closed symbols, and low resistance bilayers, shown with open symbols in Fig. 8. The low resistance devices have on average a significantly higher G_{ae} than the high resistance devices. In addition, the variation of G_{ae} with R/R_N is much more dramatic for the low resistance devices, and furthermore

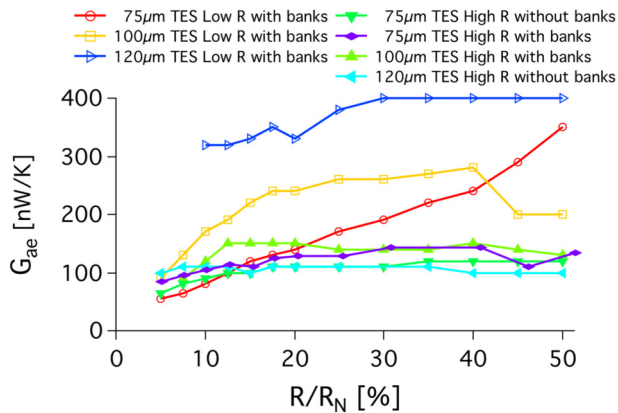


FIG. 8. Fitted G_{ae} as a function of the bias point R/R_N for TESs of different sizes with $T_{bath} = 55$ mK, some with and some without banks, with high or low resistance bilayers.

there appears to be a size dependence of the variation with R/R_N . Larger devices show smaller changes in G_{ae} through the superconducting transition.

V. DISCUSSION

A. Applicability of the two-body model

The two-body model satisfactorily fits the experimental data over a wide range of bias points, TES sizes, and bath temperatures, despite the underlying simplifications and assumptions discussed above. This implies that the key physics of our devices is being captured, namely, that the excess noise observed in these devices is dominated by an internal thermal fluctuation noise between a large heat capacity we associate with the absorber connected by a finite thermal conductance to a small heat capacity we associate with the TES. The reduction in the excess noise observed with increasing bath temperature is captured within this model, because as T_{bath} is increased, the thermal response time of the TES increases, while the time constant of the internal thermal fluctuations remains relatively constant. Thus, as T_{bath} approaches T_c , the TES current becomes too slow to respond to the relatively fast internal thermal fluctuations between the two bodies, and therefore, P_{ae} becomes less significant. This also explains the observed reduction in excess noise (M^2/α) between the $120\ \mu\text{m}$ and $75\ \mu\text{m}$ high resistance devices shown in Figs. 4 and 5, respectively. G_{bath} has been shown to be proportional to the TES perimeter³¹ and, therefore, is significantly smaller in the $75\ \mu\text{m}$ device than the $120\ \mu\text{m}$ device. This smaller G_{bath} in the $75\ \mu\text{m}$ device leads to a longer effective response time of the TES, and therefore, this TES is less sensitive to internal thermal fluctuations. These dependencies of the various noise terms on the TES parameters were well described by Maasilta.²⁴

B. Origin of the finite G_{ae} term

The two-body model appears to be consistent with the measured data in the studied devices. Now, we must consider the origin of the finite thermal conductance between the two bodies that gives

rise to the internal thermal fluctuation noise. The absorber of our devices is thermally connected to the superconducting bilayer by two gold pillar stems. The stems are $10\ \mu\text{m}$ in diameter and approximately $4\ \mu\text{m}$ high. Using these dimensions and the measured resistivity ($\sim 1\ \text{n}\Omega\text{m}$) of this gold layer, the electrical resistance of each stem is approximately $50\ \mu\Omega$. Using the Wiedemann–Franz law, we can estimate the electronic contribution to the total thermal conductance from the absorber to the edge of the TES is approximately $90\ \mu\text{W/K}$. This is approximately three orders of magnitude larger than G_{ae} used to fit the high resistance devices. This suggests the pillar stems are not the limiting thermal conductance in our system. In addition, if the limiting thermal conductance in our system were from the pillar stems, one would expect similar fitted values of G_{ae} for all devices, since the pillar stem dimensions are the same. In contrast, we observe a stark difference between the fitted G_{ae} for high resistance and low resistance bilayers.

The interface between the pillar stems and the bilayer may also be a limiting point in the thermal conductance between the absorber and the TES since each is fabricated independently. If the transmissivity of the interface between the stem and the TES is sufficiently poor that there is an insulating boundary between the two, then we must consider the impact of electron–phonon coupling between the two bodies and within the TES. This coupling is limited by the TES volume and, therefore, might be expected to vary with the TES bilayer thickness, as observed. However, the order of magnitude of the electron–phonon coupling conductance can be estimated from $n_{ep}\Sigma_{ep}VT_c^{n_{ep}-1}$, where n_{ep} is approximately 5, V is the volume of the TES bilayer, and $\Sigma_{ep} \sim 2 \times 10^9\ \text{W/m}^3\text{K}^4$ is the electron–phonon coupling parameter.³² Using these values, we estimated the electron–phonon thermal conductance to be $\sim 2\ \text{nW/K}$ for the $120\ \mu\text{m}$ low resistance device, which has the largest volume and, therefore, highest electron–phonon thermal conductance. This is around two orders of magnitude smaller than the fitted G_{ae} . Also, one would expect to see a strong dependence of the fitted G_{ae} on the TES size, which is not seen in our fitted parameters. Therefore, we exclude this as the limiting thermal conductance.

As discussed in Sec. II, the absorber is made up of a Bi layer above a Au layer. Therefore, the interface between these two layers could also be a possible origin of a finite thermal conductance in the system. However, this would mean that in our model, C_e would include the heat capacity of the TES and the large heat capacity of the Au layer, and C_a would only include the small heat capacity of the Bi layer. Such a rearrangement of the heat capacity in the system would produce very different behavior to that shown in the model discussed above, and we found we were unable to fit the measured noise and complex impedance data for any values of G_{ae} .

The final possibility we consider is that the limiting thermal conductance between our two bodies is the finite thermal conductance of the TES bilayer itself. The normal state sheet resistance of the high and low resistance bilayers just above T_c was measured as 50 and $13\ \text{m}\Omega/\square$, respectively. Using the Wiedemann–Franz law, these values correspond to a thermal conductance of approximately $50\ \text{nW/K}$ and $170\ \text{nW/K}$ for our approximately square TES devices. These values are in reasonable agreement with the average G_{ae} fitted for both our high resistance and low resistance devices, and this is suggestive that the bilayer itself may be the origin of the limiting thermal conductance.

However, this is only an estimate of the normal state thermal conductance of the bilayer. When the TES is within the superconducting transition, the situation is likely more complicated. Some regions of the TES may be superconducting, while others are in the normal state. In addition, the formation of cooper pairs within the bilayer reduces the quasiparticle density of states at the Fermi energy, and therefore, the thermal conductance of the film is expected to decrease as the bilayer transitions further into the superconducting state at lower R/R_N . This may explain the small reduction in G_{ae} observed in all devices at small R/R_N . However, explanation of the larger variations observed in the fitted G_{ae} with R/R_N observed in the low resistance devices will require a sophisticated theoretical description of the superconducting transition, which so far has not been achieved. One intuitive explanation for this behavior, however, is that this is a consequence of the superconducting proximity effect of Nb electrical leads to the TES.

It has been shown that Nb leads on the TES heavily influence the superconducting order parameter within the TES, and as a result, the TES may act as a Josephson-like weak-link between the two leads.³³ The degree to which the TES behaves as a weak-link has been shown to be dependent on the TES size, with smaller devices more strongly affected by the proximity effect than larger devices.^{33,34} Hence, we speculate that in the low resistance devices, the large variation in G_{ae} seen in the $75\mu\text{m}$ device compared with the $120\mu\text{m}$ device may be a consequence of the greater influence of Nb leads on the electrical properties of the TES. Similarly, this may be the reason for the observation of the smaller variation in G_{ae} with R/R_N in high resistance devices compared with low resistance devices. The degree to which the proximity effect from the leads is expected to influence the bilayer is expected to be dependent on the resistance of the bilayer through the variation in the mean-free path of electrons. Thus, one would expect a smaller proximity effect in the high resistance devices. Assuming that the variation in G_{ae} does indeed depend on the proximity effect from the leads, then we would also expect smaller variations for higher resistance bilayers, as observed.

Note that in the analysis presented here, TES temperature T is assumed to be a constant, independent of bath temperature and bias point. T is taken as the measured T_c of each device. In reality, T varies, but only by $\sim 1\%$ over the range of bias points and bath temperatures considered in this work, and therefore, this assumption does not have a significant impact on the conclusions drawn. In particular, the variation in T cannot account for the variation in the fitted G_{ae} with R/R_N in our devices.

Based on the analysis presented above, we postulate that the finite internal thermal conductance responsible for the observed internal thermal fluctuation noise is from the TES itself. However, this means that the finite G_{ae} is found within the TES body in our two-body electrothermal model, and not independent of the TES body as shown in Fig. 2 and used in the noise calculations. This may indicate that the element we have associated with the TES in Fig. 2(b) is actually only a small fraction of the total bilayer area. It is shown in the supplementary material that the model is quite insensitive to the magnitude of C_e and, therefore, would be insensitive to such distinctions. Therefore, a future study of more sophisticated many-body models will be needed to fully determine how the physical elements must be divided into a precise model.

C. Additional noise sources

The two-body model presented here assumes that there is no contribution from additional noise sources, such as higher order terms in the nonequilibrium Johnson noise. This assumption appears reasonable for the devices presented so far, given the ability to fit wide ranging noise and complex impedance data with G_{ae} that closely match expectations for the thermal conductance of the bilayer film. However, we cannot exclude the possibility that there are additional noise terms that give small contributions in the studied cases. Indeed, previous experimental data for Mo/Cu devices showed much larger excess noise contributions than seen here despite similar bilayer sheet resistances.¹¹ In addition, it has been shown before that around regions of rapidly changing α , so-called kinks, the excess noise may be significantly larger than observed here,⁸ and may be larger than that predicted from similar thermal models. In the devices studied here, it has been shown previously that kinks are much less prevalent than in previous designs with additional normal metal features on top of the bilayer.¹⁰ Therefore, while our model has been successful at describing the origin of the excess noise in these devices over a wide range of R/R_N , it is likely that in other designs additional noise mechanisms may be present.

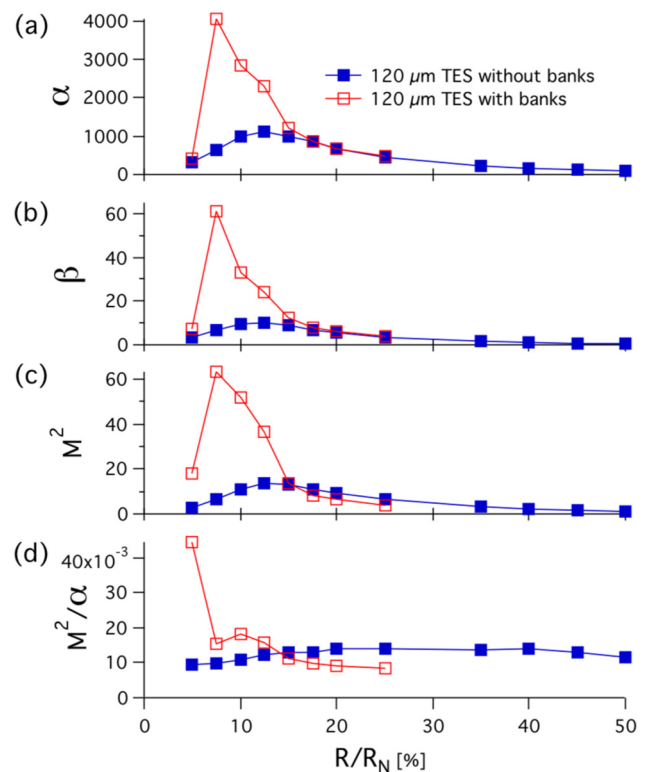


FIG. 9. Noise and transition parameters extracted by fitting the single-body model to data from $120\mu\text{m}$ high resistance TESs with (red, open) and without (blue, closed) banks as a function of the bias point in the transition R/R_N taken at $T_{\text{bath}} = 55\text{mK}$. Transition parameters (a) α and (b) β extracted from complex impedance measurements. (c) Excess noise parameter M^2 . (d) Ratio of M^2/α .

As an illustration of a possible additional noise source or mechanism beyond the two-body model consider the data presented in Fig. 9 for a $120\text{ }\mu\text{m}$ high resistance TES with banks. Figures 9(a)–9(c) show $\alpha(R/R_N)$, $\beta(R/R_N)$, $M^2(R/R_N)$, respectively, for this device with banks compared with the device without banks discussed above. Notice that around $7.5\%R_N$, α increases dramatically, reaching ~ 4000 . This suggests the presence of a kink, as has been seen in other similar devices low in the transition.¹⁰ Figure 9(c) shows that the excess noise parameter in the vicinity of that bias point is also extremely large. Figure 9(d) shows that around this kink M^2/α is also very large. This large deviation from the broad correlation between α and M^2 has been seen before around these kink features.⁸

Figure 10 shows the measured noise in this $120\text{ }\mu\text{m}$ high resistance TES with banks when biased close to the kink at $R/R_N = 5\%$. We have attempted to fit the measured noise with the single-body and two-body models described above, as shown in the figure. In the two-body model, while the magnitude of the noise in the 1–100 kHz region of interest may be captured if G_{ae} is extremely low (9 nW/K), it does not correctly predict the roll-off of noise at higher frequencies. However, with an additional Johnson noise contribution (MJ_{tes}) added to the single-body model, we are able to describe the measured data. This is suggestive that in this region, there is an additional noise source that may be related to the Johnson noise. This noise source may have been dominant in devices from previous studies, particularly those with additional normal metal features on the TES bilayer where kinks are more prevalent, but as discussed above in the other devices presented in this article it does not appear to contribute significantly. At bias points well above the kink ($>15\%R_N$), the excess noise in the

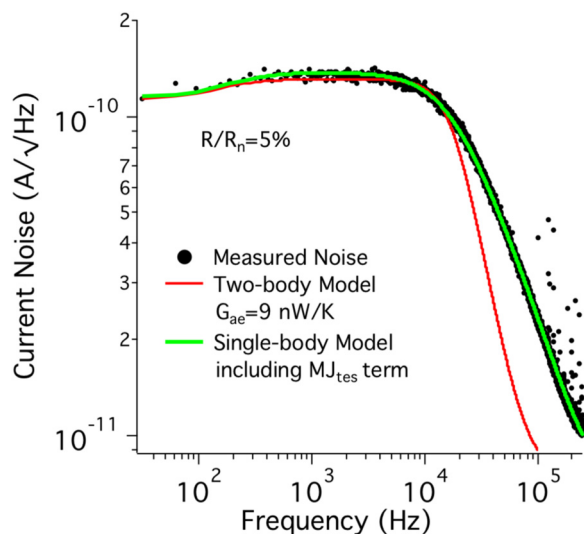


FIG. 10. Noise spectra for a $120\text{ }\mu\text{m}$ high resistance TES with banks biased at $R/R_N = 5\%$, $T_{bath} = 55\text{ mK}$. Black points show the measured noise data. Red line shows best fit to data using the two-body model. Green line shows the calculated noise using the single-body model including an excess noise contribution of the form MJ_{tes} .

device with banks shown in Fig. 9 is in reasonable agreement with the device with no banks, and the noise spectra can once again be fit with the two-body model. These observations suggest that around a kink in the transition, as well as an internal thermal fluctuation noise, there may be a distinct additional noise mechanism.

VI. CONCLUSION

In conclusion, we have shown that in various TES devices with Mo/Au bilayers, the measured noise is consistent with a two-body model describing an internal thermal fluctuation noise arising from a finite thermal conductance between the absorber and the TES bilayer. The fitted value of the internal thermal conductance is comparable to expectations for the normal thermal conductance of the bilayer of the TES for both low resistance and high resistance cases. The internal thermal conductance is found to decrease when the TES is biased lower in the superconducting transition, consistent with the expectation of a loss of density of states as the bilayer becomes more superconducting. This effect is found to be more dramatic in devices with greater proximity effect from the superconducting Nb leads. Finally, we have shown that this two-body model is able to account for excess noise in many devices over several bias points and bath temperatures. However, around regions of large and rapidly changing α additional noise sources related to the Johnson noise may be dominant.

These conclusions indicate that the internal thermal conductance of the TES bilayer is an important factor in the design of a TES microcalorimeter for optimal performance for a given application. The detectors discussed in this article typically have an energy resolution of $\sim 2\text{ eV}$. However, when all other parameters are fixed, the difference in the predicted energy resolution between the low resistance and high resistance bilayers can be as large as $\sim 0.3\text{ eV}$. Eliminating all noise in excess of the single-body prediction could lead to a further improvement in the energy resolution of $\sim 0.2\text{ eV}$. Therefore, minimization of the internal thermal fluctuation noise may have a significant impact on the achieved energy resolution. These considerations are particularly relevant to the application of frequency division multiplexed readout of large arrays of TESs. It was recently shown that the degradation of performance from this multiplexing scheme can be mitigated by the use of high resistance TESs.^{35,36} This implies that there may be a trade-off between optimization of the TES resistance for low noise and good multiplexed performance.

SUPPLEMENTARY MATERIAL

See the [supplementary material](#) for the figure showing the impact of C_e on the two-body model fit shown in Fig. 3(c).

ACKNOWLEDGMENTS

The authors wish to thank NASA's Astrophysics Division for their generous support of this work. This work was performed in part under the auspices of the U.S. Department of Energy (DOE) by Lawrence Livermore National Laboratory under Contract No. DE-AC52-07NA27344.

REFERENCES

- ¹M. K. Bacrania, A. S. Hoover, P. J. Karpus, M. W. Rabin, C. R. Rudy, D. T. Vo, J. A. Beall, D. A. Bennett, W. B. Doriese, G. C. Hilton, R. D. Horansky, K. D. Irwin, N. Jethava, E. Sassi, J. N. Ullom, and L. R. Vale, *IEEE Trans. Nucl. Sci.* **56**, 2299 (2009).
- ²C. Isaila, F. Feilitzsch, J. Höhne, C. Hollerith, K. Phelan, B. Simmnacher, R. Weiland, and D. Wernicke, *Nucl. Instrum. Methods Phys. Res. Sect. A* **559**, 734 (2006).
- ³J. W. Fowler, B. K. Alpert, D. A. Bennett, W. B. Doriese, J. D. Gard, G. C. Hilton, L. T. Hudson, Y.-I. Joe, K. M. Morgan, G. C. O'Neil, C. D. Reintsema, D. R. Schmidt, D. S. Swetz, C. I. Szabo, and J. N. Ullom, *Metrologia* **54**, 494 (2017).
- ⁴S. Okada, D. A. Bennett, W. B. Doriese, J. W. Fowler, K. D. Irwin, S. Ishimoto, M. Sato, D. R. Schmidt, D. S. Swetz, H. Tatsuno, J. N. Ullom, and S. Yamada, *J. Low Temp. Phys.* **176**, 1015 (2014).
- ⁵D. Barret, T. L. Trong, J.-W. den Herder, L. Piro, X. Barcons, J. Huovelin, R. Kelley, J. M. Mas-Hesse, K. Mitsuda, S. Paltani, G. Rauw, A. Rožanska, J. Wilms, M. Barbera, E. Bozzo, M. T. Ceballos, I. Charles, A. Decourchelle, R. den Hartog, J.-M. Duval, F. Fiore, F. Gatti, A. Goldwurm, B. Jackson, P. Jonker, C. Kilbourne, C. Macculi, M. Mendez, S. Molendi, P. Orleanski, F. Pajot, E. Pointecouteau, F. Porter, G. W. Pratt, D. Prêle, L. Ravera, E. Renotte, J. Schaye, K. Shinozaki, L. Valenziano, J. Vink, N. Webb, N. Yamasaki, F. Delcelier-Douchin, M. L. Du, J.-M. Mesnager, A. Pradines, G. Branduardi-Raymont, M. Dadina, A. Finoguenov, Y. Fukazawa, A. Janiuk, J. Miller, Y. Nazé, F. Nicastro, S. Sciortino, J. M. Torrejon, H. Geoffroy, I. Hernandez, L. Luno, P. Peille, J. André, C. Daniel, C. Etcheverry, E. Gloaguen, J. Hassin, G. Hervet, I. Maussang, J. Moeuza, A. Paillet, B. Vella, G. C. Garrido, J.-C. Damery, C. Panem, J. Panh, S. Bandler, J.-M. Biffi, K. Boyce, A. Clénet, M. DiPirro, P. Jamotton, S. Lotti, D. Schwander, S. Smith, B.-J. van Leeuwen, H. van Weers, T. Brand, B. Cobo, T. Dauser, J. de Plaa, and E. Cucchetti, *Proc. SPIE* **9905**, 99052F (2016).
- ⁶J. A. Gaskin, R. Allured, S. R. Bandler, S. Basso, M. W. Bautz, M. F. Baysinger, M. P. Biskach, T. M. Boswell, P. D. Capizzo, K.-W. Chan, M. M. Civitani, L. M. Cohen, V. Cotroneo, J. M. Davis, C. T. DeRoo, M. J. DiPirro, A. Dominguez, L. L. Fabisinski, A. D. Falcone, E. Figueroa-Feliciano, J. C. Garcia, K. E. Gelmis, R. K. Heilmann, R. C. Hopkins, T. Jackson, K. Kilaru, R. P. Kraft, T. Liu, R. S. McClelland, R. L. McEntaffer, K. S. McCarley, J. A. Mulqueen, F. Özel, G. Pareschi, P. B. Reid, R. E. Riveros, M. A. Rodriguez, J. W. Rowe, T. T. Saha, M. L. Schattenburg, A. R. Schnell, D. A. Schwartz, P. M. Solly, R. M. Suggs, S. G. Sutherlin, D. A. Swartz, S. Trolrier-McKinstry, J. H. Tutt, A. Vikhlinin, J. Walker, W. Yoon, and W. W. Zhang, *Proc. SPIE* **10397**, 103970S (2017).
- ⁷J. Ullom, W. Doriese, G. Hilton, J. Beall, S. Deiker, K. Irwin, C. Reintsema, L. Vale, and Y. Xu, *Nucl. Instrum. Methods Phys. Res. Sect. A* **520**, 333 (2004).
- ⁸S. J. Smith, J. S. Adams, C. N. Bailey, S. R. Bandler, S. E. Busch, J. A. Chervenak, M. E. Eckart, F. M. Finkbeiner, C. A. Kilbourne, R. L. Kelley, S.-J. Lee, J.-P. Porst, F. S. Porter, and J. E. Sadleir, *J. Appl. Phys.* **114**, 074513 (2013).
- ⁹D. A. Wollman, K. D. Irwin, G. C. Hilton, L. L. Dulcie, D. E. Newbury, and J. M. Martinis, *J. Microsc.* **188**, 196 (2003).
- ¹⁰N. A. Wakeham, J. S. Adams, S. R. Bandler, J. A. Chervenak, A. M. Datesman, M. E. Eckart, F. M. Finkbeiner, R. L. Kelley, C. A. Kilbourne, A. R. Miniussi, F. S. Porter, J. E. Sadleir, K. Sakai, S. J. Smith, E. J. Wassell, and W. Yoon, *J. Low Temp. Phys.* **193**, 231 (2018).
- ¹¹N. Jethava, J. N. Ullom, K. D. Irwin, W. B. Doriese, J. A. Beall, G. C. Hilton, L. R. Vale, and B. Zink, *AIP Conf. Proc.* **1185**, 31 (2009).
- ¹²M. Lindeman, "Microcalorimetry and the transition-edge sensor," Ph.D. thesis (University of California at Davis, 2000).
- ¹³E. Figueroa-Feliciano, *J. Appl. Phys.* **99**, 114513 (2006).
- ¹⁴K. Irwin, *Nucl. Instrum. Methods Phys. Res. Sect. A* **559**, 718 (2006).
- ¹⁵C. M. Knoedler, *J. Appl. Phys.* **54**, 2773 (1983).
- ¹⁶D. A. Bennett, D. R. Schmidt, D. S. Swetz, and J. N. Ullom, *Appl. Phys. Lett.* **104**, 042602 (2014).
- ¹⁷M. Galeazzi, *IEEE Trans. Appl. Supercond.* **21**, 267 (2011).
- ¹⁸H. Hoevers, A. Bento, M. Bruijn, L. Gottardi, M. Korevaar, W. Mels, and P. de Korte, *Nucl. Instrum. Methods Phys. Res. Sect. A* **444**, 192 (2000).
- ¹⁹M. R. J. Palosaari, K. M. Kinnunen, M. L. Ridder, J. van der Kuur, H. F. C. Hoevers, and I. J. Maasilta, *J. Low Temp. Phys.* **167**, 129 (2012).
- ²⁰Y. Takei, L. Gottardi, H. F. C. Hoevers, P. A. J. de Korte, J. van der Kuur, M. L. Ridder, and M. P. Bruijn, *J. Low Temp. Phys.* **151**, 161 (2008).
- ²¹K. M. Kinnunen, M. R. J. Palosaari, and I. J. Maasilta, *J. Appl. Phys.* **112**, 034515 (2012).
- ²²A. R. Miniussi, J. S. Adams, S. R. Bandler, J. A. Chervenak, A. M. Datesman, M. E. Eckart, A. J. Ewin, F. M. Finkbeiner, R. L. Kelley, C. A. Kilbourne, F. S. Porter, J. E. Sadleir, K. Sakai, S. J. Smith, N. A. Wakeham, E. J. Wassell, and W. Yoon, *J. Low Temp. Phys.* **193**, 337 (2018).
- ²³M. Durkin, J. S. Adams, S. R. Bandler, J. A. Chervenak, E. V. Denison, W. B. Doriese, S. M. Duff, F. M. Finkbeiner, J. W. Fowler, J. D. Gard, G. C. Hilton, K. D. Irwin, Y. I. Joe, R. L. Kelley, C. A. Kilbourne, A. R. Miniussi, K. M. Morgan, G. C. O'Neil, C. G. Pappas, F. S. Porter, C. D. Reintsema, D. A. Rudman, K. Sakai, S. J. Smith, R. W. Stevens, D. S. Swetz, P. Szypryt, J. N. Ullom, L. R. Vale, N. Wakeham, and J. C. Weber, "Demonstration of Athena X-IFU Compatible 40-Row Time-Division-Multiplexed Readout," *IEEE Trans. Appl. Superconduct.* (published online, 2019).
- ²⁴I. J. Maasilta, *AIP Adv.* **2**, 042110 (2012).
- ²⁵M. A. Lindeman, S. Bandler, R. P. Brekosky, J. A. Chervenak, E. Figueroa-Feliciano, F. M. Finkbeiner, M. J. Li, and C. A. Kilbourne, *Rev. Sci. Instrum.* **75**, 1283 (2004).
- ²⁶K. D. Irwin and G. C. Hilton, *Cryogenic Particle Detection* (Springer, 2005), Vol. 99.
- ²⁷W. S. Boyle and K. F. Rodgers, *J. Opt. Soc. Am.* **49**, 66 (1959).
- ²⁸D. McCammon, "Thermal equilibrium calorimeters—An introduction," in *Cryogenic Particle Detection*, edited by C. Enss (Springer Berlin Heidelberg, Berlin, Heidelberg, 2005), pp. 1–34.
- ²⁹M. E. Eckart, J. S. Adams, S. R. Bandler, R. P. Brekosky, J. A. Chervenak, F. M. Finkbeiner, R. L. Kelley, C. A. Kilbourne, F. Scott Porter, J. E. Sadleir, and S. J. Smith, *AIP Conf. Proc.* **1185**, 430 (2009).
- ³⁰A. Kozorezov, A. Golubov, D. Martin, P. Verhoeve, and J. K. Wigmore, *AIP Conf. Proc.* **1185**, 27 (2009).
- ³¹J. P. Hays-Wehle, D. R. Schmidt, J. N. Ullom, and D. S. Swetz, *J. Low Temp. Phys.* **184**, 492 (2016).
- ³²F. C. Wellstood, C. Urbina, and J. Clarke, *Phys. Rev. B* **49**, 5942 (1994).
- ³³J. E. Sadleir, S. J. Smith, S. R. Bandler, J. A. Chervenak, and J. R. Clem, *Phys. Rev. Lett.* **104**, 047003 (2010).
- ³⁴J. E. Sadleir, S. J. Smith, I. K. Robinson, F. M. Finkbeiner, J. A. Chervenak, S. R. Bandler, M. E. Eckart, and C. A. Kilbourne, *Phys. Rev. B* **84**, 184502 (2011).
- ³⁵L. Gottardi, S. J. Smith, A. Kozorezov, H. Akamatsu, J. van der Kuur, S. R. Bandler, M. P. Bruijn, J. A. Chervenak, J. R. Gao, R. H. den Hartog, B. D. Jackson, P. Khosropanah, A. Miniussi, K. Nagayoshi, M. Ridder, J. Sadleir, K. Sakai, and N. Wakeham, *J. Low Temp. Phys.* **193**, 209 (2018).
- ³⁶K. Sakai, J. S. Adams, S. R. Bandler, J. A. Chervenak, A. M. Datesman, M. E. Eckart, F. M. Finkbeiner, R. L. Kelley, C. A. Kilbourne, A. R. Miniussi, F. S. Porter, J. S. Sadleir, S. J. Smith, N. A. Wakeham, E. J. Wassell, W. Yoon, H. Akamatsu, M. P. Bruijn, L. Gottardi, B. D. Jackson, J. van der Kuur, B. J. van Leeuwen, A. J. van der Linden, H. J. vanWeers, and M. Kiviranta, *J. Low Temp. Phys.* **193**, 356 (2018).